

Photogrammetric set-up for the analysis of particle motion in aerosol under microgravity conditions

This content has been downloaded from IOPscience. Please scroll down to see the full text.

1999 Meas. Sci. Technol. 10 921

(<http://iopscience.iop.org/0957-0233/10/10/313>)

View [the table of contents for this issue](#), or go to the [journal homepage](#) for more

Download details:

IP Address: 136.186.1.81

This content was downloaded on 06/09/2015 at 00:26

Please note that [terms and conditions apply](#).

Photogrammetric set-up for the analysis of particle motion in aerosol under microgravity conditions

O Dupont[†], F Dubois[†], A Vedernikov[†], J C Legros[†], J Willneff[‡]
and C Lockowandt[§]

[†] Université Libre de Bruxelles, Microgravity Research Centre, CP 165/62; 50 av F D Roosevelt, 1050 Bruxelles, Belgium

[‡] Institute of Geodesy and Photogrammetry, ETH-Hoenggerberg CH-8093 Zurich, Switzerland

[§] Swedish Space Corporation, Albygatan 107, S-171 04 Solna, Sweden

E-mail: odupont@ulb.ac.be, willneff@geod.ethz.ch and clo@ssc.se

Received 23 February 1999, in final form and accepted for publication 13 July 1999

Abstract. An optical set-up to investigate the motion of aerosol particles under microgravity conditions has been designed and manufactured. It provides accurate measurement of 3D coordinates of up to 1000 particles, discrimination between particles of different nature and estimation of the angular velocity of small aerosol crystals. A photogrammetric technique is applied to track independently moving particles, using the acquisition and processing of stereoscopic image sequences. The optical scheme of the set-up is based on a unique objective that collects the light coming from different directions from the back- and front-illuminated aerosol, and transfers it to four different cameras. Driving parameters for the optical head design and image quality are discussed. The set-up performance was verified on optical test objects, aerosol simulators and also real aerosol under microgravity conditions during parabolic flight. The set-up has been designed for use in the JET experiment on board the Maser 8 sounding rocket. The experiment aims at the first direct observation of the chemojet motion of free-flying small growing crystals. Investigation of chemojet motion along with elaboration of the image analysis technique is focused on the development of highly sensitive, real-time, non-perturbative analysis of the reactions on the surface of aerosol particles.

Keywords: 3D particle tracking, 3D velocimetry, photogrammetry, crystal growth

1. Introduction

Aerosols proliferate in natural and technogenic processes, filling the Earth's atmosphere and cosmic space. Usually, aerosols are in a nonequilibrium state, the particles having some kind of physico-chemical interaction with the gas; such as sublimation, absorption, or a topochemical or catalytic reaction. It was shown recently that, in such cases, free-flying aerosol particles undergo not only random but also oriented momentum exchange with the gas atoms/molecules (Vedernikov and Melikhov 1994, Melikhov and Vedernikov 1995). The latter arises because the rate of any process is non-uniform along the surface of a particle and is time dependent. Although chemojet motion can be much more intensive than Brownian motion, it is still very weak. The accuracy of determination of the chemojet motion parameters is extremely sensitive to gravity because of the hydrodynamic influence of sedimentation. Only broad features can be estimated on Earth. Experimentation in microgravity conditions removes this limitation and allows us not only to investigate this new phenomenon but also

to develop on its basis a highly sensitive, real-time, non-perturbative research tool for the analysis of reactions on the surface of aerosol particles. This paper describes the optical concept, its design and hardware, as well as the photogrammetric method to be used in the JET experiment aiming to investigate chemojet motion. The experiment is to be realized in a European Space Agency (ESA) module for the Maser 8 sounding rocket developed by the Swedish Space Corporation to be launched in 1999 at Esrange, Sweden.

Peculiarities of the JET experiment are briefly described in section 2, where the scientific requirements for the optical set-up are formulated.

Section 3 deals with 3D particle tracking velocimetry (3D PTV), which was found to be the most suitable measurement technique. It allows one to track independently moving particles and to measure the velocity distribution functions of two kinds of particles, presenting elastic and inelastic collisions respectively. 3D PTV can be considered as a typical application field of digital photogrammetry involving the acquisition and processing of stereoscopic image sequences of moving particles. The reactor chamber

(RC) is viewed from four different directions to avoid ambiguities and to obtain a high tracking reliability of long particle trajectories. Thus, the spatial coordinates of each particle are retrieved by triangulation between the simultaneously recorded images. The velocity of each particle is straightforwardly computed using the particle displacements calculated from successive maps of particle positions and the time delay t_{acq} between them. Such measurements give rise to an accurate estimation of the 3D velocities and this approach thus yields an individual identification of the particles, unlike the Doppler method.

A description of the imaging system, light source and general architecture of the sounding rocket module is given in section 4. The optical design is based on a special configuration that allows us to simultaneously record four pictures of the RC with a unique objective collecting the light from different directions and transferring it to the different cameras with the help of a set of mirrors. The experiment chamber is illuminated from two sides along the optical axis. Background illumination is used to determine the positions of the particles in the visualized volume of the RC. Front illumination facilitates discrimination between reference particles and crystals as well as yielding information about rotation of the aerosol crystals.

The set-up performance was verified on several optical test objects, aerosol simulators, and also real aerosol under microgravity conditions during parabolic flight. Results of the experimental tests are presented in section 5. It was found that the optical system and photogrammetric technique meet the scientific requirements.

2. Description of the experimental system

The primary goal of the JET experiment is to carry out the first direct observation of chemojet motion and to verify the available theoretical model. Crystal growth by physical vapour transport is chosen as an example of the physico-chemical process responsible for the oriented momentum exchange between gas and aerosol particles. In this experiment the aerosol comprises two types of particles of about the same size—urotropine crystals and glass balloons coated with gold. The latter do not grow under the conditions of the experiment and are used as reference particles, not subject to chemojet motion. Urotropine monocrystals are colourless, having various prismatic shapes with flat faces. The change of their size during the experiment is estimated to be less than 30%. Both types of particles are prepared on Earth and placed in a special container providing separate storage of each particle in a closed microscopic volume. The particles are injected at the beginning of the experimental run. The total number of particles in the container does not exceed 1024.

The process is investigated in a parallelepipedic RC filled with a binary mixture of urotropine vapour and argon. Two opposite faces of the chamber are used for the visualization of the aerosol, two other faces are for the particle container, injection unit and mechanical elements, while the last two opposite faces are connected to the source of urotropine vapour. Oversaturated urotropine vapour concentration is created shortly before the launch of the rocket in order to

provide crystal growth. After the beginning of microgravity conditions, both types of particle are injected into the RC where they are visualized by the optical unit. The images of the aerosol are recorded by an onboard video recorder and transmitted to Earth in real time through a telemetry channel.

Theoretical analysis shows that crystals exhibiting chemojet motion should have a random distribution of velocity vectors in space, a high spread of velocity values and time variation of both transitional and rotational motion. In particular, some of the crystals will rotate and have negligible transitional component, some will move almost linearly, and some will stay at rest. Such probabilistic behaviour requires motion analysis of a relatively large number of particles.

This is the first time that chemojet motion has been investigated in microgravity conditions, where it should dominate over other types of motion. Consequently, one can expect a high deviation of the actual experimental values from the theoretical predictions. In addition, one cannot exclude the presence of components other than chemojet motion due to microgravity disturbances, electrostatic charging, Brownian transitional and rotational movement, etc. Therefore, the motion of the particles has to be analysed by versatile methods and with high accuracy.

The following inequality has to be satisfied:

$$L_{3D} \gg d > v_c t_{acq} \geq \delta r \quad (1)$$

where L_{3D} is the mean distance between particles in the aerosol, d is the mean crystal size, v_c is the mean expected crystal velocity due to the chemojet motion, t_{acq} is the acquisition period, and δr is the error of the particle coordinate determination. The inequality (1) requires that the concentration of the number of particles, the acquisition period and the error of the particle coordinate determination should be low enough to detect displacements less than the particle size and to track trajectory changes of each particle moving independently in the region where collisions are negligible.

Taking into account heat and mass transport limitations, the main experimental parameters are found to be as follows. Mean crystal size is about 40×10^{-6} m with mean expected velocity v_c of the order of 50×10^{-6} m s⁻¹. Mean diameter of the reference particles is about 60×10^{-6} m. The RC subjected to visual analysis is 14×10^{-3} m height, 11×10^{-3} m wide and 10×10^{-3} m deep along the optical axis. The space density of the particles in the aerosol is expected to be no higher than 400 cm⁻³, which gives $L_{3D} = 1.4 \times 10^{-3}$ m. To meet the inequality expressed in equation (1), the acquisition time t_{acq} is taken to be 0.2 s.

Bearing in mind the above-mentioned quantitative parameters, the optical unit and image processing system should provide the following major functions:

- Accurate measurement of the 3D coordinates of each aerosol particle in the experimental volume, the total number of which will not exceed 1000.
- Discrimination between the two types of particles.
- Discrimination between rotating and non-rotating crystals.

3. The photogrammetric method

With the development of solid state sensor imaging devices and powerful computer platforms, new image processing techniques providing solutions for a large number of 3D measurement tasks have become possible in the past two decades. While computer vision often deals with qualitative image understanding tasks, digital photogrammetry aims at the derivation of accurate 3D metric information from digital images (Grün 1994). By the use of self-calibrating bundle adjustment techniques, 3D object coordinates are determined from multiple images of a scene, simultaneously with the measurement of the camera parameters such as the CCD orientation and CCD calibration.

The basic equation of photogrammetric 3D coordinate determination is the collinearity equation (see, e.g., Slama 1980), which simply states that object point, camera projective centre and image point lie on a straight line. This mathematical formulation has to be extended to meet the physical realities. Effects caused by lens distortion and analogue-to-digital conversion are usually compensated for by a set of additional parameters. These have to be determined in the system calibration together with the parameters of orientation of the cameras with respect to the scene and related to the non-homotetic relation between the scene and its image (distortions). Lens distortion is compensated for by a set of five additional parameters modelling radial and decentring distortion (Brown 1971). Compensation for electronic effects, generally the unknown difference between the pixel rate of a camera and the clock rate of a frame grabber, is often achieved with an affine transformation using two parameters (El-Hakim 1986). The complete set of parameters has to be determined in a system calibration before, during or after the image acquisition of an actual measurement task. The most flexible way of determining this set of parameters is the self-calibrating bundle adjustment (Brown 1976), where the 3D object coordinates, camera orientation data and camera calibration parameters are determined simultaneously, based only on image coordinate measurements and at least one scale information in object space.

3.1. The mathematical model

The fundamental mathematical theorem of photogrammetric 3D particle coordinate determination is the collinearity condition, which states that object point, camera projective centre and image point lie in a straight line (figure 1). This mathematical formulation, containing three coordinates X_0, Y_0, Z_0 of the projective centre and three angles ω, φ, κ describing the direction of the optical axes, applies to a pinhole camera model and does not consider any optical distortions. Therefore, this mathematical approach has to be extended to meet the physical realities by introducing the following parameters and model extensions:

- The camera constant c_{st} (computational imaging width).
- The principal point coordinates x_H, y_H , which show strong deviations from the sensor centre in the chosen camera design.

- Different clock rates between camera and frame grabber, causing a horizontal scale factor s_x , which deviates from one.
- The different windows in the optical paths causing a twice-broken beam to be handled in the collinearity equation.
- Compensation of the lens distortion: usually a part of the camera calibration. This effect can be neglected here due to the specifications of the chosen lens system (see section 4).

All these effects are strictly modelled in the 3D PTV implementation. The parameters c_{st}, x_H, y_H, s_x and the lens distortion are used to model the camera and are the elements of the interior orientation. The exterior orientation is the set of the six parameters $X_0, Y_0, Z_0, \omega, \varphi, \kappa$ describing the location and orientation of the camera referring to the object coordinate system. The mathematical model can be used in three different modes.

- Spatial resection: the parameters of the exterior orientation $X_0, Y_0, Z_0, \omega, \varphi, \kappa$ and the camera model c_{st}, x_H, y_H, s_x are determined in the calibration procedure from images of a reference body.
- Spatial intersection: after calibration of the system and the establishment of multi-view correspondences, 3D particle coordinates can be determined based on the orientation and camera model parameters.
- Bundle adjustment: using multiple images of a scene from each camera, taken under different orientations, object point coordinates, camera orientation parameters and camera model parameters can be determined simultaneously, based only on image space information and a minimum of one size information in object space to retrieve the magnification factor.

3.2. Data processing

Figure 2 outlines the data flow of 3D PTV data processing. The subtraction of a background image without tracers grabbed at the beginning of each sequence is the first step of the fully automatic data processing chain. Its purpose is to eliminate the global contrast and to remove some inhomogeneities of the background intensity introduced by effects of the illumination. After that, particles can be detected by thresholding, and their location in image space can be determined with subpixel accuracy by a centroid operator. In order to split particles which are partly overlapping in an image, a modified thresholding operator has been developed which searches for local maxima in the images and splits overlapping particle images at local minima (Maas 1992). The most critical step of the automatic data processing is the establishment of stereoscopic correspondences between different images of an object. Particle features (like size, shape, and colour) do not usually allow for a reliable distinction between matching candidates. Furthermore, the imaging process influences these features. Thus the only information that can be used for the establishment of correspondences is the geometric information provided by the epipolar line. Knowing the orientation parameters of the cameras from the calibration

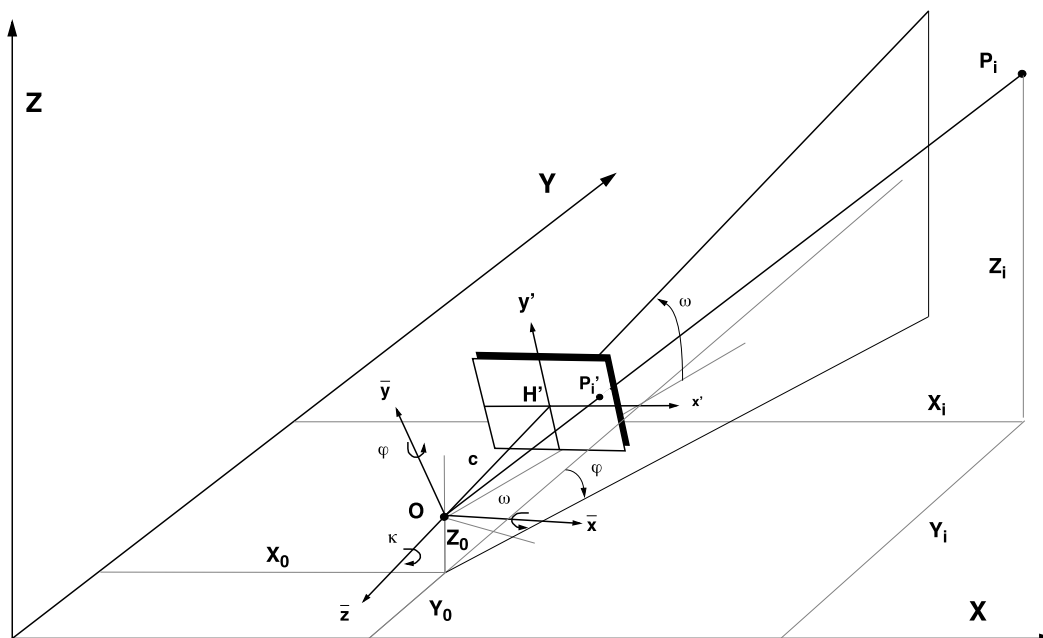


Figure 1. Definition of the mathematical symbols used in the photogrammetric method.

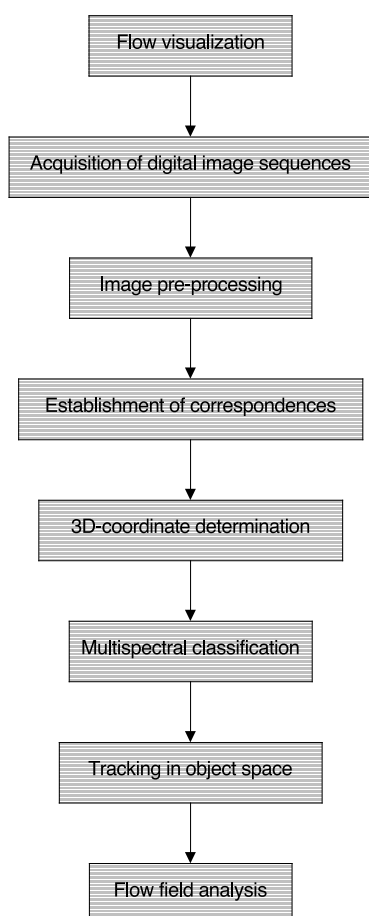


Figure 2. Data flows of the 3D particle tracking velocimetry.

procedure, proceeding from a point P' in one image, an epipolar line in another image can be defined on which

the corresponding point has to be found. The length of the line can be restricted if approximate knowledge about the depth range in object space is available. Adding a tolerance width to this epipolar line segment, the search area for the corresponding particle image becomes a narrow 2D window in image space. However, with a large number of particles there may be multiple candidates on an epipolar line. Regarding the possible ambiguities, the chosen four-camera arrangement can be considered as ideal: it reduces the number of remaining ambiguities to almost zero, and it even allows a reliable determination of most of those particles which are completely hidden in one of the four images (Maas 1996).

In the next step, the 3D coordinates of all particles can be determined by spatial intersection. The standard deviations of the determined coordinates in planimetry and depth are depending on the intersection angle of the homologous rays. Due to the volume limitation of the sounding rocket module, the optimal camera arrangement (90° angles between the optical axes) could not be realized (Virant and Dracos 1996). The redundant information provided by the three- or four-times measurement of two image coordinates for the determination of three object space coordinates allows us to perform a least-squares adjustment for each individual point, thus providing additional precision estimates. The photogrammetric determination of particle coordinates is described elsewhere (Maas *et al* 1993, Maas and Grün 1995). As fewer ambiguities can be expected when tracking is performed in 3D space, the establishment of temporal correspondences (tracking) is the last step in the processing chain outlined here. The principle of the temporal tracking is similar to the treatment of spatial ambiguities during the establishment of multi-image correspondences. Proceeding from a particle position at a time instant t_i , a search volume around an approximate location at time instant t_{i+1} is calculated using some rough pre-knowledge about the flow

under examination. If a local correlation of velocity vectors can be assumed, this information can be used to suppress the ambiguities. Furthermore, possibly available information on maximum expected Lagrangian accelerations can be used to propagate possible links into the sets of data at time instant t_{i+2} , t_{i+3} , etc, where a reduced search volume can be defined. Possible links between t_i and t_{i+1} can thus be confirmed or rejected. The tracking procedure is described in more detail by Papantoniou and Dracos (1989) and Malik *et al* (1993).

3.3. The potential of 3D PTV

With an image format of 720×576 pixels, the method allows the determination of velocity vectors of more than 1000 particles per time instant using a four-camera system (Stüer *et al* 1999, Stüer, 1999). The relative accuracy of the vector components are approximately 1:4000 (the standard deviation of X and Y coordinates over the field of view); the accuracy of the depth component Z is typically a factor of two to three worse than the components perpendicular to the main viewing direction. These figures are valid under controlled conditions. Sub-optimal illumination conditions, complex flows, temperature gradients or image noise may lead to a severe degradation of the potential. In addition to the 3D vector fields, PTV is also capable of determining particle trajectories, when storage capacity for image sequences is available. The length of the trajectories also depends on the seeding density. With a lower number of particles in the observation volume the probability of 'losing' particles due to unsolved ambiguities in the detection, the establishment of correspondences or in the tracking procedure, decreases. In practice, particles could be traced over several hundred frames if the number of particles in the observation volume was kept small. For a statistically reliable analysis of particle movement, long particle trajectories with a sufficient density over the whole object volume have to be determined. Due to the bounded number of particles in the particle bin the loss of data is reduced to a minimum by the use of four cameras (Virant and Dracos 1996).

4. Optical design

3D PTV requires that the RC be viewed from four different directions (see figure 3). All of the views are used to retrieve the 3D coordinates of the particles, and one view to discriminate reference particles from crystals. Two optical windows limit the volume of the RC along the z -axis. The angle between the viewing directions and the z -axis is fixed to 22.5° due to mechanical constraints linked to the design of the RC. The available surface to fix the RC and its related equipment, the illumination and the imaging modules is limited to the flange of the sounding rocket that has a diameter of 0.4 m.

Several optical configurations were identified to simultaneously record different pictures of the RC. We list them in the order of increasing use of common optical elements between the optical paths. The first is the standard optical set-up used in photogrammetry where a CCD camera with its optics is used for each viewing direction. This leads to an optical layout comprised of four CCDs and

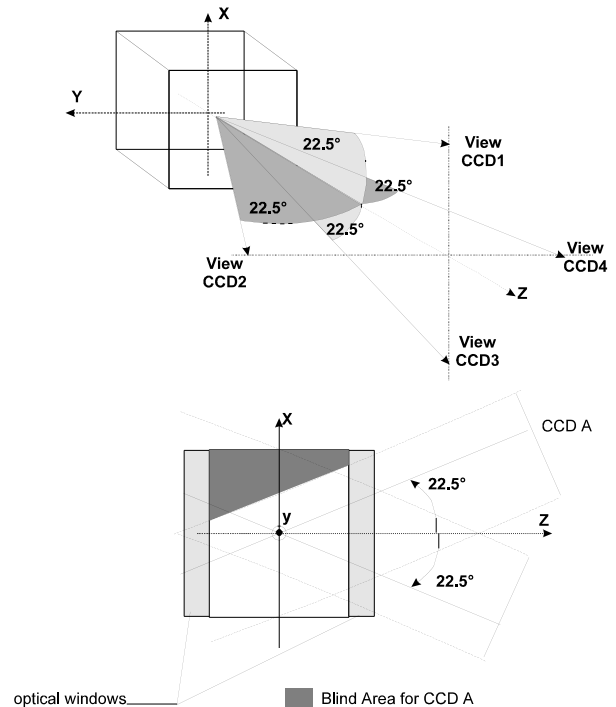


Figure 3. Viewing direction with respect to the experiment chamber.

four objectives. In the second arrangement the number of objectives is reduced to one, which collects light from different directions and transfers it to the different cameras with the help of a set of mirrors. The third arrangement involves the replacement of the multiple standard cameras by a unique high-resolution ($1k \times 1k$ pixel) CCD array, portions of which are used for the different images. This third optical layout leads to a very compact and mechanically rigid system but its drawback is the high data rate downlink from the rocket to the Earth. Thus it was the second solution that we selected, as being the best compromise between the optical requirements, mass and volume reduction and data handling.

Both background and front illumination of the RC has to be used, to meet contradictory scientific requirements. Background illumination is used for the determination of the position of all the particles in the visualization volume. Front illumination makes it possible to discriminate between reference particles and crystals on the basis of the optimization of the colour reflected by the reference particles and absorbed or transmitted by the growing crystals. This is achieved by adding coloured filters in front of the sources and of the CCD. A thermal analysis of the illumination subsystem is performed in order to prevent overheating of the experiment chamber, which could disturb crystal growth.

4.1. The imaging subsystem

The optical concept selected uses a central objective, placed on the z -axis, which images the RC to the four different cameras. Four mirrors, placed at mid-distance between the RC and the objective, redirect the optical paths into the objective. Behind the objective, a set of five mirrors redirects the optical paths to the cameras. Figure 4 shows

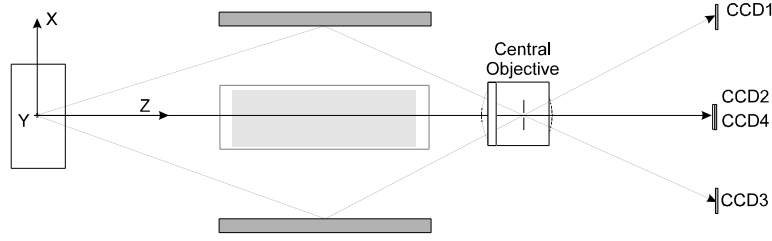


Figure 4. Schematic of the arrangement of the optical imaging head.

the arrangement of the imaging head. The advantages of the configuration are that the imaged middle plane of the RC is perpendicular to the z -axis and common to all images and the depth of focus is minimized. Although the optical system gives images with different viewing angles, there are small geometrical distortions. The front plane of the RC keeps its rectangular shape. Finally, the use of a one-piece optical head reduces the possible misalignment that can arise during lift-off of the rocket and the images recorded with the asynchronous Sony CCDs, triggered on an external synchronization signal, are multiplexed and transmitted to Earth via a standard video channel.

Because the RC is viewed at an angle of 22.5° , a lateral wall (figure 3) masks a part of the internal volume for each viewing direction. The unmasked mid-section of the RC has 9.86×10^{-3} m times 6.86×10^{-3} m. This area has to be imaged on the $\frac{1}{2}$ " CCD chip of 6.4×10^{-3} m times 4.8×10^{-3} m leading to a magnification factor m fixed to -0.67 . The focal length of the objective is driven by the necessary back focal length required to separate the images and to mechanically place the four cameras. The Sony CCDs have a square front section of 44×10^{-3} m side length. Therefore, the minimum distance between the objective and the front side of the cameras must be at least equal to 106.5 mm. This leads to a minimum focal length of 65.3 mm, easily computed knowing the magnification factor and the imaging distance. The definitive focal length is fixed at 69 mm to provide flexibility for the optical alignments. The central objective has to cover a field of view of 47° . A modified EL-Nikkor objective with focal length of 75 mm is the core of the imaging system: the two modifications are the replacement of the adjustable iris by a fixed aperture to avoid problems with vibrations during rocket lift-off and the addition of a plano-convex lens to reduce the total focal length to 69 mm.

The magnification ratio $m = -0.67$ and the large depth of focus requirement of 10^{-2} m impose that the optical aperture has to be as small as possible. However, in such configuration, diffraction effects increase the point spread function and it is necessary to find a trade-off between the geometrical and the diffraction constraints. As the aperture of the lens is small, the thin lens approximation is valid and we alleviate aberration problems. Starting from the basic geometrical optics expressing the relation between the focal length f , the object distance s_1 , the image distance s_2 and the magnification factor $m = s_2/s_1$, we have

$$\begin{aligned} s_1 &= \frac{1-m}{m}f \\ s_2 &= (1-m)f. \end{aligned} \quad (2)$$

Let us assume that the object distance increases by half of the experiment chamber length (half length = e). Then, for a particle located at the distance $s_1 + e$, the imaging distance will be $s_2 + e'$, where e' is computed with the help of equation (2) under the assumption that e and e' are small with respect to s_1 and s_2 :

$$e' = -me. \quad (3)$$

For a specified aperture diameter a , geometrical considerations give the diameter c of the circle of confusion (geometrical defocus due to the change of the object distance $s_1 + e$ with respect to the imaging distance s_2):

$$c = \frac{-mea}{(1-m)f - em}. \quad (4)$$

Replacing f/a by F_n (the f -number of the optical system), and as me can be considered small with respect to $(1-m)f$, equation (4) becomes:

$$c = \frac{-me}{(1-m)F_n}. \quad (5)$$

From another point of view, as the aperture of an imaging optical system is reduced, the image spot diameter of an illuminating point source increases due to diffraction. This can be described in a realistic way by the Airy width given by

$$A = 2\lambda(1-m)F_n \quad (6)$$

where λ is the averaged optical wavelength. The geometrical defocus increases as F_n decreases and the diffraction spot size increases with F_n . Therefore, the optimal situation occurs when $c = A$. Thus,

$$F_n = \sqrt{\frac{-me}{2(1-m)^2\lambda}}. \quad (7)$$

In the JET configuration, this leads to a $F_n = 35$ with the half reactor length $e = -5 \times 10^{-3}$ m and $m = -0.67$.

A critical requirement is to estimate the contrast ratio expected during the experiment. As we are working with a background illumination, the particles will be dark on a white background. The contrast ratio is defined as the maximum intensity drop due to the presence of a particle over the intensity of the background, as shown in figure 5.

Let us denote the minimum intensity in the area of a particle image by I_P and the intensity of the background by I_{MAX} . The contrast is defined by:

$$C = \frac{I_{MAX} - I_P}{I_{MAX}}. \quad (8)$$

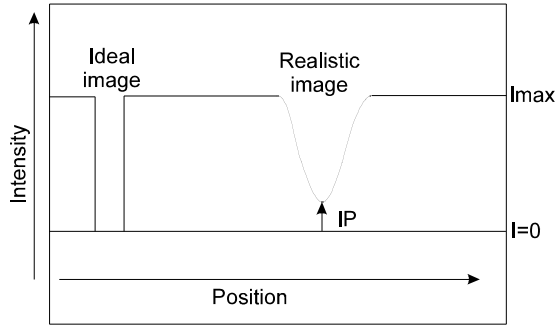


Figure 5. Definition of the particle image contrast.

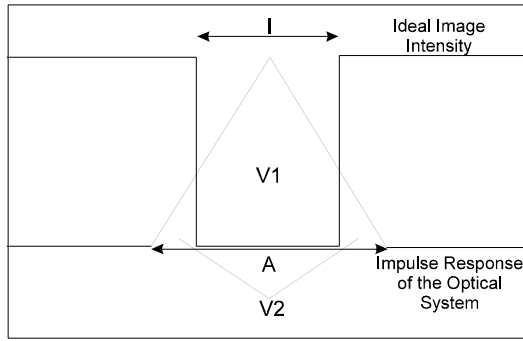


Figure 6. Estimation of the contrast ratio due to impulse response of the imaging system.

The ideal image contrast of a particle illuminated by background lighting is 1. However, the image enlargement due to the diffraction and a defocus from the depth of focus tolerance leads to a convolution process that decreases the contrast. We first evaluate the contrast ratio due to the diffraction process.

An incoherent imaging system is characterized by the impulse response of the optical system:

$$I_{realistic}(x, y) = \iint p(x - x', y - y') I_{ideal}(x', y') dx' dy' \quad (9)$$

where $p(x, y)$ is the impulse response due to diffraction. Its width is related to the Airy diameter A and for the sake of simplicity we assume that it presents a conical shape. The particles have a diameter of $40 \mu\text{m}$ and are imaged with a magnification ratio of -0.67 . Therefore, the diameter of an ideal image of a particle is $l = 26.8 \mu\text{m}$. With $F_n = 35$, the Airy disc $A = 58 \mu\text{m}$ is larger than l and the contrast is expected to be smaller than 1 (figure 6).

When the impulse response is perfectly aligned on the ideal image of a particle, the cylinder defined by the boundary of the perfect image separates the volume of the conical impulse response into two sub-volumes, V_1 and V_2 , according to whether they are inside or outside the cylinder. Geometrical considerations allow us to obtain that:

$$C = 1 - \frac{V_2}{V_1 + V_2}. \quad (10)$$

By replacing V_1 and V_2 with the usual expressions of geometry yields

$$C = \frac{3l^2 A - 2l^3}{A^3}. \quad (11)$$

With $l = 26.8 \mu\text{m}$, $A = 58 \mu\text{m}$ ($F_n = 35$), we obtain $C = 0.44$. The reduction of the contrast due to a defocus is obtained in a very similar way, except that the impulse response is a cylinder with a width given by equation (5).

Thus, when $c = 57.3 \mu\text{m}$ ($F_n = 35$), the contrast will be $C = 0.2$. As the diameter of the confusion circle is zero in the centre of the cell and as it increases when approaching the window of the cell, the contrast ratio due to a defocus will depend on the position of the particle inside the cell. Due to the fact that the impulse response resulting from a defocus is a disc, the combination of the diffraction and defocus effects near the window gives a contrast level mainly determined by the defocus effect. The combination of defocus and diffraction leads to a contrast decreasing from 0.55 (when the particle is perfectly focused in the median plane of the cell) to approximately 0.2 (particle located on the window).

The role of the contrast is of importance to the accuracy of determination of the positions of the particles. As we are working with a background illumination, the particle detection uses images with inverted contrast in order to have bright particles on a dark background. If the recording system is adjusted to use the full range of 255 grey levels, the contrast ratio will reduce the number of available grey levels according to

$$N_{grey} = 255C. \quad (12)$$

The requested accuracy on the position (half-crystal size or $20 \mu\text{m}$) requires us to use a sub-pixel accuracy measurement (about $\frac{1}{4}$ pixel) based on measurement of the barycentre of light distribution. Reduction of the number of available grey levels increases digitization noise. Estimates show that the error of the position determination is proportional to C^{-1} .

However, the problem of reduced accuracy due to the contrast can partially be overcome. By using a digitizer with an adjustable range of digitization levels, it is possible to take advantage of the full contrast range of the particles images.

4.2. The illumination and particle discrimination subsystem

The illumination system includes back and front illumination of two different ranges of colour. The purpose of the two types of illumination is to discriminate JET-sensitive and reference particles using the difference in surface characteristics: reference particles give rise to higher-intensity retrodiffused light. In this scheme, the discrimination of the particles is based on an intensity analysis which compares the maximum intensity with respect to a threshold: i.e. if retrodiffused light is higher than the threshold, a particle will be identified as a reference particle, and as an active particle otherwise. For this purpose high-quality coloured filters are used.

One type of filter is placed in the path of the front illumination and in front of the corresponding CCD image plane. Another type is used with the back illumination and the three remaining CCD image planes. The two types of filter are selected to reduce the crosstalk intensity to less than 1%.

The light source is a quartz tungsten halogen lamp of 150 W coupled to a 'one-split-in-two' fibre bundle, reducing the constraints on the source position with respect to the optical head.

A thermal analysis was performed on the illumination module. The quartz tungsten halogen light source generates heat that burns the input plane of the light bundle and perturbs the thermal regulation of the RC. Because the rocket module is at very low pressure during the experiment run, no forced airflow can be used to cool down the system. Therefore, the heat capacity of the lamp and filters housing was used to absorb the heat given off by conduction and an anti-caloric device made by the stacking of different filters blocks the heat radiated. The light emitted by the lamp first crosses a 'hot mirror' that reflects radiation between 800 and 1050 nm, then a water volume that absorbs wavelength above 1050 nm and then the Schott KG2 anti-caloric filter, 3 mm thick. The hot mirror and the KG2 filter also serve as windows for the water volume. Figure 7 shows the mechanical design of the illumination subassembly. The selection of the coloured filters for the particle discrimination is based on the spectral range of the quartz tungsten halogen light source and on the spectral response of the CCD camera. A set of filters from Schott was selected: a short-wavelength filter (Schott BG12) for the back illumination and a long-wavelength filter (Schott OG550) for the front illumination.

4.3. Implementation of the optical head in the JET module

A general view of the optical head is given in figure 8. The modified objective occupies the central position. To the left of it, four mirrors reflect the four viewing directions towards the objective. The light bundle extremity providing the front illumination is placed along the z -axis between the mirrors. It is bent in such a way that no obstruction is caused to the four fields of views. Behind the objective, four mirrors, positioned in a plane at 45° with respect to the z -axis, reflect the light to the four cameras. A fifth mirror is added to serve the fourth camera in the space previously left free between the CCDs 1, 2 and 3. The optical head is a parallelepiped of 80×10^{-3} m times 80×10^{-3} m front surface and 210×10^{-3} m long from the output plane of the light bundle to the end of the CCD block. The four cameras are attached by four independent and adjustable brackets to the structure.

The cameras are synchronized and the images are captured simultaneously by all four cameras. The images are stored in four separate memories and multiplexed to a standard video signal. A fifth image is also multiplexed into the video signal. This image contains a binary sequence code that is used as a time code during the analysis of the images. The video sequence is stored on S-VHS videotape by the onboard video recorder. All functions are controlled with an onboard computer that can be pre-programmed for various experiment profiles or operated in real time via telecommand. The computer also functions as a data acquisition system storing all relevant data.

The experiment is positioned in front of the optical head (see figure 9). The RC has two windows. The front window is the observation window and also serves as an inlet for the front illumination. The back window is used

for the back illumination. The windows have double and triple glasses (the interior window is sapphire) for optimal thermal properties. The particle bin is placed along one of the sides that are opened to the injection system. Crystals and reference particles are kept there before injection. The compartments of source of reagent gas (SRG) are placed at the top and bottom of the RC. Both SRG compartments are filled with urotropine powder to supply the RC with oversaturated vapour. The temperature in the SRG compartments is higher than in the RC, providing urotropine diffusive flux to the RC. Each SRG compartment ends with a bellows controlling the pressure in the experiment unit. The interfaces between the RC and the SRGs prevent particles from leaving the RC. They also play the role of a thermal barrier, maintaining a temperature difference between the RC and the SRGs of up to 25 K and temperature gradients in the RC and SRG compartments lower than 0.13 K. The experiment unit is heated with four heaters placed on the RC: one heater on each SRG and two heaters placed on the outer front window. The heaters are controlled individually. In the experiment the temperature in the RC is kept at 100°C .

At the beginning of the microgravity experiment, particles are injected in the RC with the injection unit. The latter comprises a motor/spring-controlled piston placed behind the particle bin. A spring moves the piston and the gas flow pushes particles out of the particle bin into the RC. The vortex of the gas stream contributes to a statistically uniform distribution of the particles in the RC.

The optical unit is activated shortly before the launch in order to prevent overheating of the water filter. Images of the RC are recorded throughout the period of microgravity conditions until the end of the experiment.

5. Experimental results

The experimental verification of the performance of the optical head was performed in four steps. The first step was characterization of the imaging quality and its comparison with that expected. Secondly, the performance of the photogrammetric algorithm was verified using the optical head with a reference target inserted in the RC. Finally, tests on aerosol simulators were performed on the ground and on real aerosols during parabolic flight using both hardware and software. The test results are reported sequentially.

5.1. Optical alignment and resolution tests

The optical head is screwed to the rocket flange and its position is fixed with respect to the RC. Therefore, the total distance between the mid-plane of the RC and the cameras is fixed. There are two adjustments to be made. The first is translation of the objective inside the optical head for focus adjustment. The second adjustment step is the alignment of each individual CCD with respect to the object. Due to the mechanical architecture of the system, no other adjustments are required.

The resolution of the optical system is verified with a USAF target that consists of group of line-space patterns whose spatial frequency increases as the sixth root of two. The depth of focus of the system was simultaneously verified

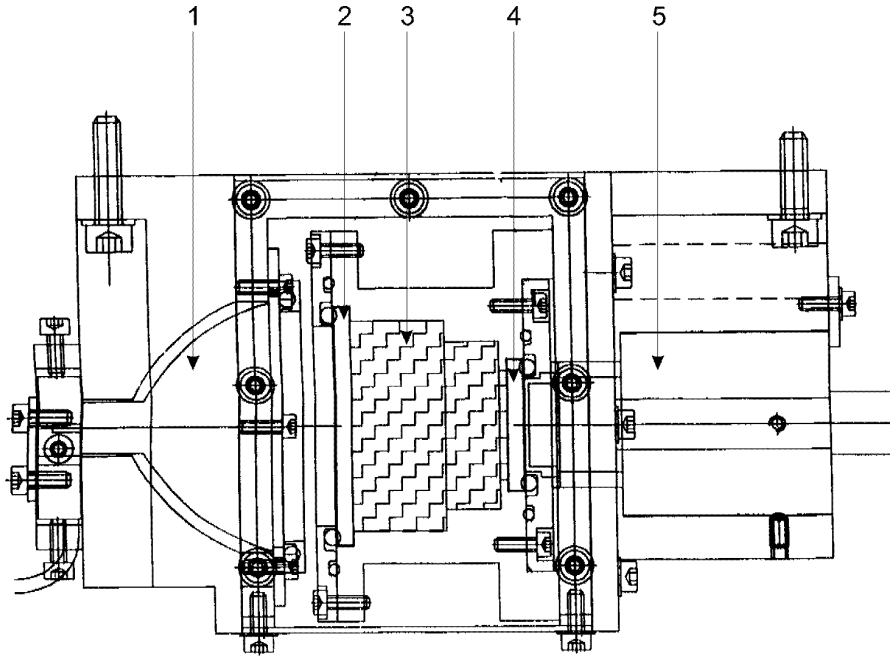


Figure 7. Mechanical design of the illumination subassembly: 1, quartz tungsten halogen lamp; 2, hot mirror; 3, water volume; 4, KG2 filter; 5, light bundle.

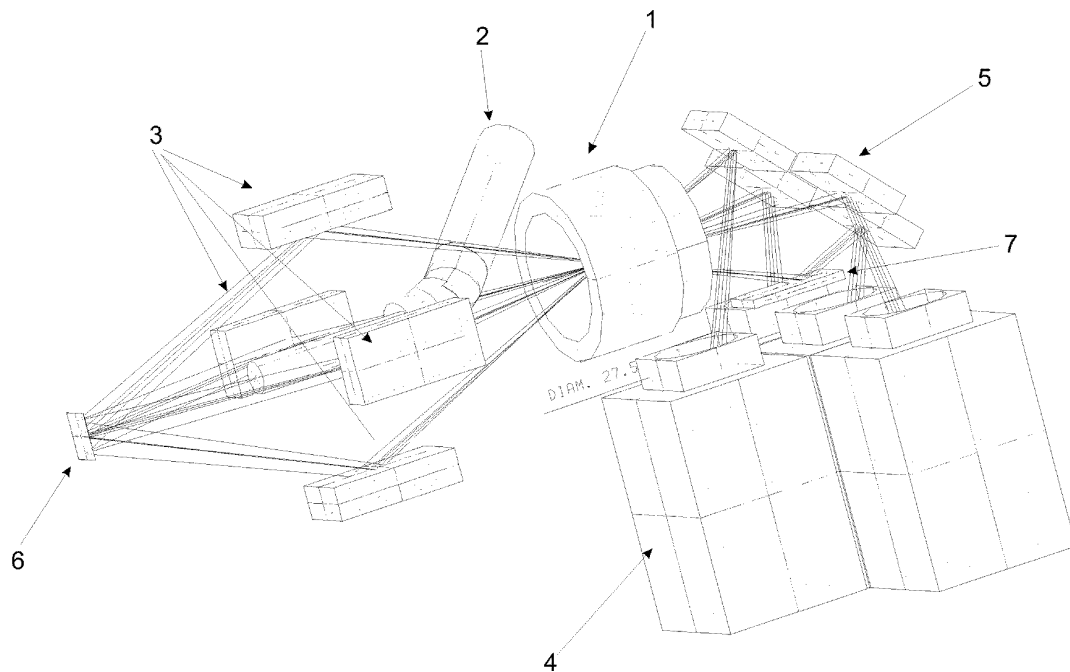


Figure 8. Mechanical design of the imaging optical head: 1, objective; 2, light bundle for front illumination; 3, mirrors; 4, CCDs; 5, mirrors; 6, RC; 7, additional mirror.

by displacing by $\pm 5 \times 10^{-3}$ m the USAF target with respect to the mid-plane of the RC. Looking to the image of the resolution target, 14.3 line pairs per millimetre are resolved leading to a resolution of $35 \mu\text{m}$ on the total depth of the experimental cell at 50% of modulation.

The resolution of the optical system is also verified by measuring two point spread functions: the first simulates the visualization of a reference particle illuminated by the front light source. This was achieved by creating a bright spot

with a $10 \mu\text{m}$ diameter pinhole illuminated from behind. The mid-height width of the point spread function is $40 \mu\text{m}$. The second simulates the visualization of particles on a bright background. This was performed by measuring the intensity distribution of a dark spot illuminated with the back-light system. The mid-height width of the point spread function is $50 \mu\text{m}$. The values are in good agreement with the value found by numerical simulations and with the resolution measured experimentally with the USAF target.

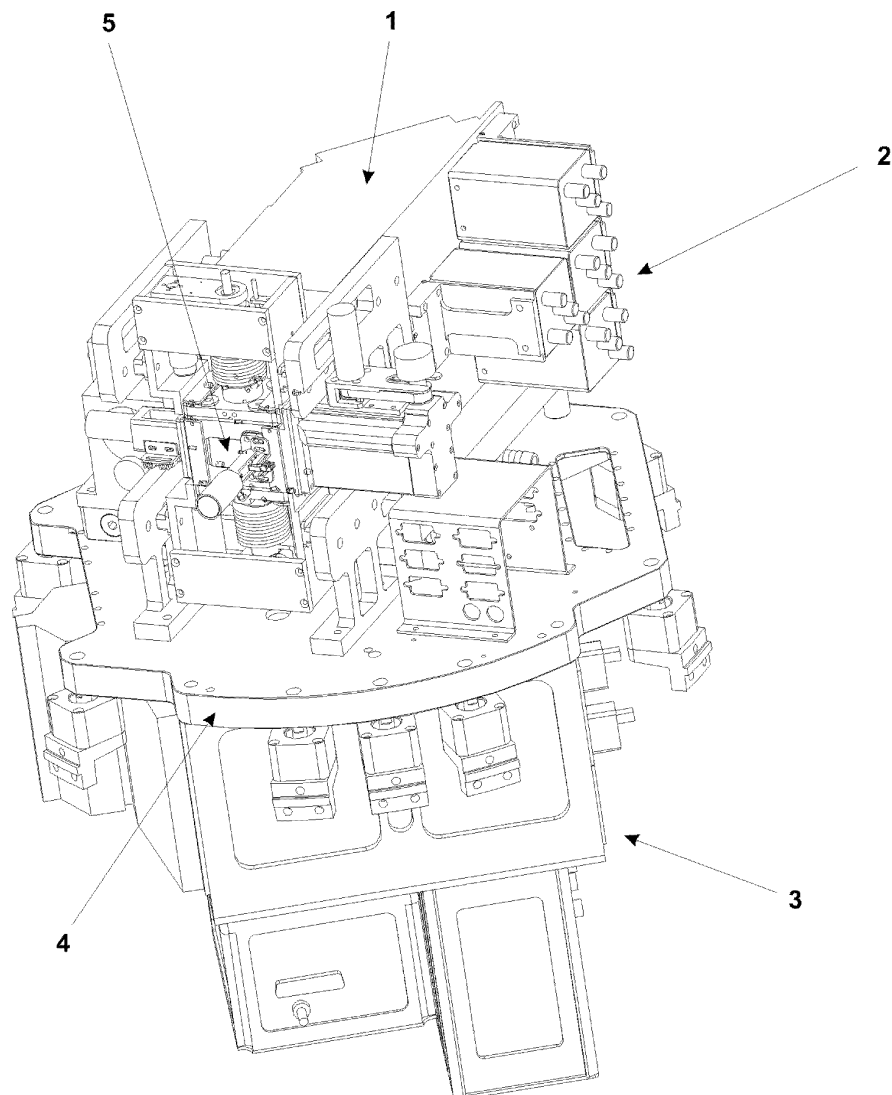


Figure 9. General view of the JET sounding rocket module: 1, optical head; 2, CCDs; 3, electronic module; 4, rocket flange; 5, RC.

Regarding the calibration of the camera, it was found that there was a strong dependence of the intensity recorded by the camera with respect to the angle and the orientation from which the light arrives. This is of crucial importance in the present design because each camera has light arriving with a different orientation: i.e. CCD 1 is illuminated from the left, CCD 2 from the right, CCD 3 from the top and CCD 4 from the bottom. Figure 10 shows that the light intensity recorded by the Sony camera depends strongly on the angle and the orientation. The experimental test conditions are: no shutter, no IR filter and manual gain at the maximum value. The behaviour of the Sony camera was also compared with cameras of other manufacturers. The tests showed that this problem is inherent to CCDs, but unfortunately the effect is more pronounced in Sony cameras.

5.2. Performance of the 3D PTV

In order to define epipolar lines for the establishment of correspondences and to compute 3D particle coordinates, the orientation and calibration parameters of the system have to

be determined in a calibration procedure. This calibration is performed by a photogrammetric technique using images of a 3D reference body with discrete targets. Using the mathematical model of spatial resection, the orientation and calibration parameters of a camera can be determined from one single image of the calibration reference body under suitable illumination, if the 3D coordinates of the targets are known.

The calibration reference body was fabricated by the spark erosion technique in aluminium with 48 mechanically generated reference points in the anodized surface. To calibrate the system in its actual configuration the calibration body should be put into the experiment cell prior to launch. A second calibration should also be performed after flight.

The four-camera system was calibrated by spatial resection using the image quadruplet shown in figure 3. As the mathematical model does not contain mirrors, the optical paths were 'unfolded' for further processing, leading to a configuration with four virtual projection centres and four virtual camera positions with a convergent camera arrangement and principal point coordinates deviating

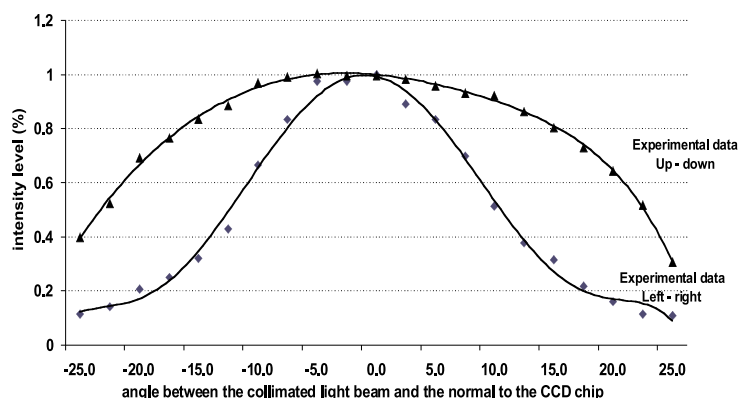


Figure 10. Calibration curve of the Sony camera.

strongly from the centre of the image.

From each calibration image, more than 20 points of the reference body were detected and used for the determination of the photogrammetric parameters. Only the central part of the reference body is in the field of view of the cameras. Those points that were detected were nearly visible in all four images. As a conclusion the observable object volume is rather small, but the field of view of the four cameras is almost identical. The calibration yielded the following results:

- The standard deviation of unit weight was between 3.16–3.52 μm for three of the four images, but for the decisive camera the value was 6.82 μm . This does not fully exploit the accuracy potential of the cameras and the method, but can be considered satisfactory.
- The camera constant could not be determined. This is due to the extremely narrow opening angle, which leads to high correlations between parameters of exterior and interior orientations. The mathematical model depicts an over-parametrization to the chosen configuration. Therefore, the camera constant can be introduced as a fixed parameter with a value of 108.83 mm computed from the parameters of the optical system, and the effects of deviations from this value are covered by parameters of the exterior orientation.
- The principal point is turned outward by between 28 and 42 mm, depending on the camera lying far outside the actual image format.
- No other significant parameters could be determined.

From the parameters of the exterior and interior orientation of the cameras and the limitation of the object volume in the z -dimension, a field of view of each camera can be calculated. The values for each camera are listed in table 1. These values are 3D coordinates referring to the position of the calibration body during the acquisition of the calibration images.

5.3. Tests on aerosol simulators

Discrimination of the two types of particles was verified with an aerosol simulator comprised of a glass plate with crystals and glass balloons on top of it. Urotropine crystals were grown directly on a glass plate from oversaturated urotropine vapour in a vacuum chamber using a two-zone technique.

Mass crystallization took place after spontaneous nucleation on the bottom window. Parameters of crystallization were adjusted to obtain crystals having a mean size and surface number density equal to the expected density during the flight. Different types of defect crystals were left on the test sample to assess their image properties: they accounted for about 20% of the total number of crystals. Crystals larger than 60 μm and most of the crystals smaller than 30 μm were removed mechanically from the glass window. Then, reference particles were added on the test sample. The size and quality of each particle was analysed with a microscope to relate them to the images obtained with the optical head.

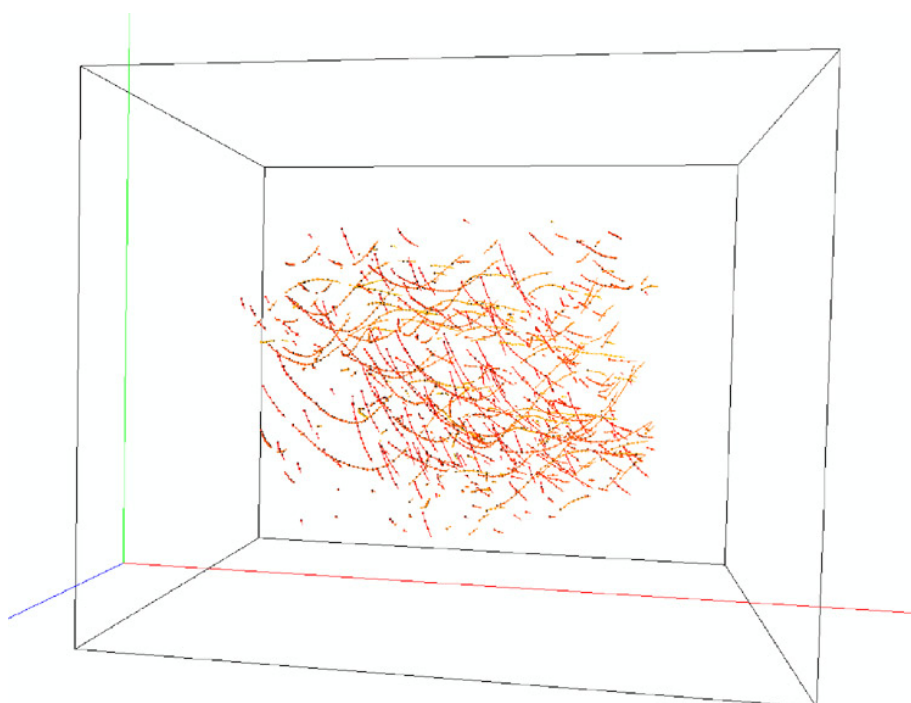
It was found that the intensity of the light reflected by reference particles changes in quite a restricted range, being always above the background level. Variation of intensity was produced by change of the shape of the reference particles and uniformity of the coating. This leads to the necessity of accurate pre-flight control of the particle shapes and quality of coating.

About 95% of the crystalline particles are seen as dark spots on a grey background. For specific orientations (within an angle variation of less than 5°), crystals produce bright spots on the image. The intensity of such reflections lies within a wide range up to saturation level. It is supposed that such a high level of reflected intensity results from the full internal reflections from the inside surfaces of crystal faces and/or in combination with reflections from the glass windows. Some of the crystals have reflection intensity within the range of brightness of reference particles. The mean number of crystals that may be confused with reference particles due to this effect is estimated to be about 5%.

In spite of all precautions, there are found to be several types of non-perfect monocrystals in the flight aerosol. This may arise because of aggregation, breaking down of the crystals during insertion, surface deterioration because of sublimation at the beginning of the introduction, formation of large-scale growth defects on the crystals during growth, etc. These types of defect crystals were identified in the test sample and it was found that their image properties coincide with the properties of ordinary crystals within the accuracy requirements.

Table 1. Camera fields of view.

CCD	Z minimum: 0 mm				Z maximum: 10 mm			
	Upper left	Upper right	Lower left	Lower right	Upper left	Upper right	Lower left	Lower right
1	10.9/2.2	11.0/9.5	1.2/2.3	1.3/9.5	11/-1.8	11.2/5.8	0.8/-1.8	0.9/5.9
2	9.3/0.2	9.3/7.4	—	-0.6/7.3	13.5/0.1	13.5/7.7	3.0/0.0	2.9/7.6
3	13.4/0.4	13.3/7.4	-0.6/0.2	3.4/7.4	9.5/0.3	9.5/7.8	-1.0/0.2	—
4	11/-1.6	11/5.6	3.5/0.3	1.4/5.6	11.2/2.2	11.2/10	1.0/2.3	-1.0/7.7
			1.6				1.0/10	

**Figure 11.** 3D reconstruction of particle trajectories during injection test in parabolic flight.

5.4. Tests on aerosol under microgravity conditions

The overall functioning of the optical system and 3D PTV performance was tested on real aerosol composed of one type of particles—glass balloons. In order to prevent rapid sedimentation of the particles the tests were performed in microgravity conditions during parabolic flights at Bordeaux in 1998. The parabolic flights were characterized by a relatively high level of microgravity disturbances of up to 10^{-2} – 10^{-1} g. Sometimes displacement of particles between sequential image acquisition was close to the mean distance between the particles in the aerosol: in such situations 3D PTV was not applicable. Such a problem cannot arise in the experiment on the sounding rocket, which has a higher quality of microgravity uniformity (better than 10^{-5} g). The injection system was also tested during these parabolic flights. The number of particles injected in the observation volume varied in a wide range depending on the injection parameters but was always several times lower than 1000, the limitation imposed by the 3D PTV method. Taking into account the above-mentioned facts, optical tests were mostly focused on checking general performance of the system and its accuracy, and on getting reference data before the rocket experiment.

In all, ten image sequences over around 100 time steps (which equate to 5 s in time) were analysed. Acquired before the injection, the background images were used to eliminate global contrast and to remove any variation of background light intensities from the sequence images. With this approach, the same parameters for particle detection could be used for all four cameras because the differences in the illumination were homogenized to a common level. After the image pre-processing the particles appeared as bright stains on a more or less dark background. The difference between the grey levels of the imaged particles and the background was of the order of 10–30 times. Depending on the sequence, up to 300 particles could be detected in the images and up to 170 particles could be determined per time step. The standard deviation of unit weight was 7–11 μm . The standard deviation of the 3D coordinate determination by spatial intersection was between 0.007/0.007/0.017 and 0.010/0.010/0.025 mm in X/Y/Z. The ratio between the standard deviations in depth and planimetry coordinates confirmed the predicted factor of 2.4.

After calculation of the 3D coordinates of each time step, tracking was applied to obtain trajectories in the velocity

field. An example of the resulting visualization is shown in figure 11. The density of the velocity field and the length of the trajectories varied considerably from sequence to sequence. The maximum number of tracked particles was about 100, but there were also sequences where almost no trajectories were found, which should be attributed to the periods of high-level microgravity perturbations that were mentioned at the beginning of this section.

6. Conclusions

A compact, rigid and easily adjustable optical system has been designed to obtain 3D trajectories of the microscopic aerosol particles under microgravity conditions. The 3D coordinates of crystals and reference particles are retrieved using the photogrammetric method. The discrimination between the two kinds of particles is performed optically with appropriate coloured filters.

Crystal rotation is controlled by temporal analysis of the light intensity reflected by the crystals.

The optical system provides an observation volume of about 0.6 cm^3 with a depth of focus of 10^{-2} m . The optical resolution is kept constant along the complete depth of the RC by the balancing of diffraction and defocus effects.

Evaluation of the images by 3D PTV allows one to track about 1000 independently moving particles, which is sufficiently higher than the number of particles anticipated in the observation volume of the JET experiment and the number of particles registered in the ground tests. The standard deviation of the 3D coordinate determination was found to be between 0.007 and 0.011 mm for the planimetry coordinates and from 0.017 to 0.025 mm for the coordinate along the optical axis.

Due to correlation effects, the accuracy of a velocity vector derived from a particle trajectory will be better than the accuracy of the absolute position.

The combination of the compact optical system and the photogrammetric technique have been successfully tested on the ground and during parabolic flights and are seen to meet the scientific requirements.

It is important to note that the optical system was developed to meet particular requirements of the JET experiment. Most of the above-mentioned characteristics could be considerably changed or improved for other applications.

Acknowledgments

This work was supported by the European Space Agency Prodex Programme, and by the Belgian Programme on

Interuniversity Poles of Attraction (PAI 4-06) initiated by the Belgian State, Prime Minister's Office, Federal Office for Scientific, Technical and Cultural Affairs.

References

- Brown D 1971 Close-range camera calibration *Photo. Engng* **37** 8
- 1976 The bundle adjustment—progress and prospects *IAPRS* vol 21, part 3
- El-Hakim S F 1986: Real-time image metrology with CCD cameras *Photogramm. Engng Remote Sens.* **52** 1757–66
- Grün A 1994 Digital close-range photogrammetry—progress through automation *Keynote Paper, ISPRS Com. V Symp. (Melbourne, March 1–4) IAPRS* vol 30, part V
- Maas H-G 1996 Contributions of digital photogrammetry to 3-D PTV *Three-Dimensional Velocity and Vorticity Measuring and Image Analysis Techniques* ed Th Dracos (Dordrecht: Kluwer) pp 191–207
- 1992 Complexity analysis for the determination of dense spatial target fields *Robust Computer Vision* ed Förstner and Ruwiede (Karlsruhe: Wichmann)
- Maas H-G and Grün A 1995 Digital photogrammetric techniques for high-resolution 3D flow velocity measurements *Opt. Engng* **34** 1970–6
- Maas H-G, Grün A and Papantoniou D 1993 Particle tracking in three-dimensional turbulent flows—Part I: Photogrammetric determination of particle coordinates *Exp. Fluids* **15** 133–46
- Malik N, Dracos T and Papantoniou D 1993 Particle tracking in three-dimensional turbulent flows—Part II: Particle tracking *Exp. Fluids* **15** 279–94
- Melikhov I V and Vedernikov A A 1995 Jet growth (non-Brownian) random walk of crystals in aerosols *Dokl. Phys. Chem.* **340** 505–8
- Papantoniou D and Dracos T 1989 Analysing 3-dimensional turbulent motions in open channel flow by use of stereoscopy and particle tracking *Advances in Turbulence* vol 2, ed Hernholz and Fiedler (Heidelberg: Springer)
- Slama C (ed) 1980 *Manual of Photogrammetry* (Falls Church, VA: American Society of Photogrammetry)
- Stürer H 1999 Separation on a forward facing step *PhD Thesis* Nr.13132 ETH Zurich, Switzerland
- Stürer H, Maas H-G, Virant M and Becker J 1999 A volumetric 3D measurement tool for velocity field diagnostics in micro-gravity experiments *Meas. Sci. Technol.* **10** 904
- Vedernikov A A and Melikhov I V 1994 *Motion of growing crystals in gas in short-term microgravity experiments (Proc. Int. Workshop on Short-Term Experiments under Strongly Reduced Gravity Conditions (Bremen, Germany, July 4–7))* pp 263–7
- Virant M and Dracos Th 1996 Establishment of a videogrammetric PTV system *Three-Dimensional Velocity and Vorticity Measuring and Image Analysis Techniques* ed Th Dracos (Dordrecht: Kluwer) pp 229–54